Lawrence Berkeley National Laboratory

Title

Ultrathin oxide layers for nanoscale integration of molecular light absorbers, catalysts, and complete artificial photosystems

Permalink

https://escholarship.org/uc/item/1p6019rk

Journal

The Journal of Chemical Physics, 150(4)

ISSN

0021-9606

Authors

Katsoukis, Georgios
Frei, Heinz

Publication Date

2019-01-28

DOI

10.1063/1.5052453

Peer reviewed

Ultrathin Oxide Layers for Nanoscale Integration of Molecular Light Absorbers, Catalysts and Complete Artificial Photosystems

Georgios Katsoukis and Heinz Frei[*]

Molecular Biophysics and Integrated Bioimaging Division, Lawrence Berkeley National Laboratory, University of California, Berkeley, CA 94720

HMFrei@lbl.gov

ABSTRACT

Artificial photosynthesis is an attractive approach for the generation of renewable fuels because such systems will be suitable for deployment on highly abundant, non-arable land. Recently emerged methods of nanoscience to create conformal, ultrathin oxide layers enable the hierarchical integration of light absorbers, catalysts and membranes into systems with far simpler synthetic approaches than available till now. This holds in particular for the coupling of molecular light absorbers and catalysts for sunlight to fuel conversion, providing photoelectrodes with greatly improved stability. Moreover, the use of ultrathin inert oxides as proton conducting, molecule impermeable membranes has opened up the integration of reduction and oxidation half reactions into complete photosynthetic systems on the shortest possible length scale – the nanometer scale. This capability affords minimization of energy-degrading resistance losses caused by ion transport over macroscale distances while separating the incompatible water oxidation and carbon dioxide reduction catalysis environments on the nanoscale. Understanding of charge transport between molecular components embedded in the oxide layers is critical for guiding synthetic design improvements of the light absorber-catalyst units to optimize performance, and integrate them into complete artificial photosystems. Recent results and insights from transient optical, vibrational, and photoelectrochemical studies are presented, and future challenges and

opportunities for engaging dynamic spectroscopies to accelerate the development of nanoscale integrated artificial photosystems discussed.

I. INTRODUCTION

The recent emergence of ultrathin oxide membranes enabled by the techniques of nanoscience, in particular atomic layer deposition (ALD),[1] has created unexpected opportunities for the development of efficient artificial systems for fuels from sunlight. Advances include dramatic performance improvements in terms of stability and efficiency of existing materials and designs, and the creation of entirely new concepts for solar fuels systems that could not be contemplated prior to the advent of ALD and related techniques.

One such advance made possible by ultrathin oxide layers is the protection of the surface of semiconductor light absorbers, which has opened up the use of materials with attractive optical properties as photoanodes that have been inaccessible so far due to ease of corrosion. McIntyre and Chidsey were the first to demonstrate that silicon protected by a few nanometer thick TiO_2 layer could stably perform water oxidation at an iridium metal overlayer for time periods orders of magnitude beyond those achievable in the absence of an ultrathin layer.[2,3] Titania as thick as 100 nm, coated by Ni catalyst layer, subsequently enabled Lewis and coworkers to use a variety of semiconductors with desirable bandgaps and band edge energetics as photoanodes for visible light driven water oxidation even under harsh alkaline conditions, e.g. CdTe and $BiVO_4$.[4,5] Such 'leaky TiO_2' coated GaAs, GaP and InGaP photoanodes ('leaky' referring to hole conductivity at intra-bandgap potential) were shown to operate continuously for tens to hundreds

4

of hours.[6,7] The ultrathin oxide layer not only prevents corrosive water oxidation catalysis on the semiconductor surface but passivates the light absorber by eliminating intra-bandgap defect states, thereby enhancing the photocatalytic efficiency.[8] While wide bandgap or insulator materials TiO_2, Al_2O_3 and SiO_2 are typically used as protective nanolayers, oxides of late transition metals like Co or Ni, which are established water oxidation catalysts, have also been found to exhibit a surface passivating role for visible light absorbers like $BiVO_4$, Si, or CdTe.[8,9] Therefore, these nanolayers introduce both co-catalyst and surface passivating function.

Nanometer thick oxide layers have similarly enabled remarkable performance improvement of metal catalysts relevant for artificial photosynthesis, especially for proton reduction. An early example was the observation by Domen and coworkers of strongly enhanced proton reduction yields at Rh nanoclusters for H_2 evolution attached to GaN:ZnO photocatalyst particles when encasing the Rh particle in a 2-3 nm thick layer of Cr_2O_3. Because the ultrathin oxide layer is permeable for protons and H_2, but blocks O_2, back reaction of evolving H_2 and O_2 that would otherwise readily occur on the Rh surface is prevented.[10,11] Other metal oxide nanolayers also exhibit these extremely useful transport (blocking) properties, e.g. lanthanoid and molybdenum oxide, expanding opportunities to tailor materials choices for specific photo- or electrocatalytic applications.[12,13]Amorphous silica is a unique material for blocking any species except protons and H_2 molecules. Membranes made of silica on the

order of micrometer thickness are being explored for microfuel cell applications,[14] and it has been recognized for some time that proton conductivity increases steeply for thinner, nanometer deep layers.[15] Coating of Pt particle catalysts for H^+ electroreduction to H_2 with a few nanometer thick silica shell was exploited for suppressing back reaction by blocking access of O_2, or prevent poisoning by surface access of metal ions.[16] High proton diffusivity of around 10^{-6} cm^2 s^{-1} is estimated for 2 nm thick amorphous silica layers prepared by ALD methods.[17] Protection of metal nanoparticle catalysts by ultrathin oxide coatings and progress in the application of such layers for passivating and protecting semiconductor light absorbers have recently been reviewed.[18,19]

This perspective focuses on the emerging role of ultrathin oxide layers for the development of stable and efficient *molecular* light absorber-catalyst units, and for the coupling and integration of the incompatible water oxidation and carbon dioxide reduction environments into complete nanoscale photosynthetic assemblies. Molecular, or molecularly defined, light absorbers are particularly attractive because their electronic properties can easily be tuned for the precise matching with the energetics of the catalyst they are coupled with, which is essential for converting the maximum fraction of solar photon energy into chemical energy of the fuel molecules. Emphasis of the paper is on the elucidation of photo-induced charge transfer between molecular components adsorbed on, or encapsulated in, these heterogeneous constructs by transient spectroscopy

and photoelectrochemical measurements, understanding of which is critical for guiding design improvements for enhancing efficiency.

II. ULTRATHIN SILICA SEPARATION MEMBRANE FOR NANOSCALE INTEGRATION OF ARTIFICIAL PHOTOSYSTEMS

The motivation for completing the photosynthetic process of CO_2 reduction by H_2O on the nanoscale is to avoid major energy losses of macroscale redox cycles caused by ion transport resistance and chemical side reactions, and to minimize balance of systems components. Consideration of these factors is essential for enabling scalability of artificial photosystems. Integration on the nanoscale, in turn, requires electronic coupling of the water oxidation and carbon dioxide reduction half reactions across an ultrathin membrane in order to chemically separate, but electronically and protonically connect, the mutually incompatible catalysis environments. These design aspects are realized in natural photosystems.[20,21] which embody the only existing technology for producing energy-dense chemicals at the level of terawatts, the scale needed for impact on global fuel consumption.

To address this challenge, we have developed inorganic oxide-based core-shell nanotube arrays in which each one of the independently operating nanotubes is designed to close the cycle of CO_2 reduction by H_2O on the nanoscale under membrane separation. The array geometry extends the separation of the H_2O oxidation and CO_2 reduction environments on all length

scales from nano to macro (Figure 1A,B,C).[22] As schematically shown in

Figure 1C, the core is a Co_3O_4 nanotube whose inner surface provides

efficient catalytic sites for water oxidation [17,23]

$$2 H_2O \rightarrow O_2 + 4 H^+ \tag{1}$$

The Co oxide wall thickness is around 10 nm, and tube length and diameter

can be tuned over a wide range. Currently fabricated arrays have a tube

diameter of 500 nm and are 5 µm long.[22] The very large surface area of the

dense Co_3O_4 nanotubes provides sufficient concentration of catalytic sites

per geometrical area of the array for the productive use of absorbed photons

at maximum solar intensity.[17] On the outside of the Co oxide nanotube is a 2

nm thick amorphous silica layer which chemically separates the water

oxidation environment from light absorbers. These are all-inorganic

heterobinuclear units such as ZrOCo anchored on the outside surface. Visible

light absorption occurs by metal-to-metal charge-transfer (MMCT), as shown

in Figure 1D.[24-26] In the case of ZrOCo, photoexcitation of the $Zr^{IV}OCo^{II} \rightarrow$

$Zr^{III}OCo^{III}$ state of the binuclear unit directly reduces gas phase CO_2 to CO at

the transient Zr^{III} acceptor center

$$2 CO_2 + 4 H^+ \rightarrow 2 CO + 2 H_2O \tag{2}$$

while the transient positive charge on the Co^{III} donor center is transferred

across the silica membrane to the Co_3O_4 catalyst, as will be discussed in

more detail below. The amorphous silica layer is O_2 impermeable yet readily

able to transmit protons at fluxes far exceeding those needed to avoid H^+

flux from limiting photosynthetic rates at maximum solar intensity.[16,17] This is an important property because protons generated by water oxidation on the Co oxide surface by reaction (1) need to transfer across the silica membrane to the opposite side to afford reduction of CO_2 to fuel on the tube's outside surface (reaction (2)). Hence, nanoscale silica is suitable as an ultrathin membrane for separating the incompatible environments of water vapor oxidation on the inside of each tube from that of carbon dioxide reduction outside. With the nanotubes configured in the form of an array, the reduced CO_2 products evolve in the space between the nanotubes (Figure 1A).

Tight control of electron transfer between light absorbers on the outside of the core-shell nanotube and Co oxide on the inside is accomplished by *p*-oligo(phenylene vinylene) wire molecules (3 aromatic units, abbrev. PV3) embedded in the silica membrane (Figure 1C).[29,30] HOMO and LUMO energetics of the PV3 molecules can be tuned over a large range by introducing substituents on the aryl and alkene backbone with appropriate electron donating or withdrawing groups for proper potential matching with light absorber and catalysts.[27-30] Moreover, LUMO and HOMO potentials can be selected to impart rectifying property on the charge flow across the membrane, which is critical for minimizing loss of charge by back reactions.[30,31,33]

A. Transient spectroscopy of charge transfer between light absorber and molecular wire

Transient optical and short circuit photoelectrochemical studies have provided detailed insight into electron and hole transfer pathways of the core-shell construct. To investigate the coupling of the oxo-bridged heterobinuclear light absorbers to molecular wires for hole transfer across the silica membrane to the Co oxide water oxidation catalyst, ore-shell nanoparticle constructs with spherical geometry were employed; the high surface area of aqueous colloidal solutions or dry pressed wafers of such nanoparticles afford the required spectral sensitivity for monitoring structural change and kinetics by transient optical and infrared spectroscopy. In order to gain the necessary flexibility and accuracy for surface attachment of wire molecules with desired HOMO energetics, a new synthetic approach was introduced, illustrated in Figure 2, to replace a previous single step attachment method of PV3 with built-in tripodal anchor.[27,28] The new method consists of surface attachment of a tripodal anchor, trimethoxy silyl aniline (TMSA), followed by linking of a PV3 molecular wire in a second, separate step.[31] As shown in the energy diagram of Figure 3,[34,35] the electronic properties of the wire molecule were selected such that the redox potential of the excited TiOCo or ZrOCo MMCT state is properly matched for facile hole transfer to the HOMO of PV3 while rendering unwanted electron transfer to the LUMO energetically inaccessible. The resulting rectifying property obviates the need for a molecularly defined linkage between the donor (Co) end of the binuclear unit on the silica surface and the embedded wire molecule because charge transfer in the desired direction should occur if the

distance between light absorber and PV3 is one nm or less, which is indeed observed.[31] As will be discussed in more detail in the following, group IVB metals Ti or Zr were selected as acceptor and the late transition metal Co^{II} as donor center of the oxo-bridged MMCT unit because the $Zr^{IV}OCo^{II}$ unit has been shown to drive water oxidation when directly coupled to a metal oxide nanocluster catalyst on the donor side while at the same time reducing CO_2 to CO at the Zr center upon $Zr^{IV}OCo^{II} \rightarrow Zr^{III}OCo^{III}$ excitation.[36]

Fast hole transfer upon excitation of the $Ti^{IV}OCo^{II} \rightarrow Ti^{III}OCo^{III}$ MMCT state (Figure 4A,B) was observed in preliminary experiments in which the wire molecules were merely physisorbed on the silica surface of a dry, pressed waver of nanoparticles featuring TiOCo units. As shown in Figure 4C and 4D, excitation of the light absorber with a 430 nm laser pulse resulted in the characteristic $PV3^+$ radical cation absorption between 500 and 630 nm, with the rise time limited by the duration of the 8 ns laser pulse (Figure 4D inset). To extend the lifetime to hundreds of µs, the acceptor $[Co^{III}(NH_3)_5Cl]Cl_2$ was co-adsorbed for removal of the electron of transient Ti^{III}; the electron capture by this sacrificial acceptor was manifested by the depletion of the $[Co^{III}(NH_3)_5Cl]^{2+}$ infrared bands upon continued photoexcitation under growth of NH_3 (the complex is known to dissociate upon reduction of Co^{III}).[31] When conducting the transient absorption experiment with core-shell nanoparticles with the wire molecules embedded in silica (no physisorbed wire present), the same $PV3^+$ radical cation signal was observed (Figure 4E). For these experiments, the Co_3O_4 core was replaced by silica (Figure 4A) because holes

residing on embedded PV3 wires transfer to Co oxide on the ultrafast time scale, as will be discussed in Sect. B,[33] which would prevent observation of the radical cation in the ns regime. We conclude that by proper matching of the redox energetics of heterobinuclear unit and wire molecule, and by selecting concentrations that result in average separation of the components of not more than one nm, visible light induced hole transfers from light absorber to silica embedded wire molecules proceeds within a few ns or faster despite the lack of atomically precise spatial organization of light absorber and wires. In particular, no molecularly defined linkage between the Co donor center of the TiOCo unit and PV3 is needed for photo-induced charge transfer to take place.

Tight energetic control of hole transport through the molecular wires by HOMO and LUMO energetics was further demonstrated by visible light sensitized short circuit current measurements. Hole injection from a sensitizer with its potential aligned with the HOMO of embedded PV3, such as Ru(bpy)$_3$ (bpy = bipyridyl) is readily detected while no current is observed for the same sample if the photosensitizer potential is situated within the HOMO-LUMO gap of the wire.[29] Similarly, transfer of electrons from a fixed potential source across the silica membrane was found to occur only for embedded molecular wires with energetically aligned LUMO, and not for wires with mismatched orbital energetics.[30]

Electron transfer from transient reduced Ti or Zr acceptor, generated by excitation of the MMCT chromophore, to an organic moiety was probed by

pyridine adsorbed onto silica nanoparticle surfaces featuring anchored binuclear units. FT-IR spectroscopy revealed two types of weak complexes of pyridine with the binuclear light absorber: For one complex, pyridine interacts weakly with the Zr (Ti) center as shown in Figure 5A. For the other, the organic is coordinated to Co.[32] Upon excitation of the broad $Zr^{IV}OCo^{II} \rightarrow$ $Zr^{III}OCo^{III}$ MMCT band (Figure 1D) at wavelengths around 400 nm with a ns laser pulse, electron transfer from ZrOCo to form pyridine radical anion is observed as evidenced by the transient absorption at 375 nm and bleach at 412 nm (Figure 5B). The shape reflects strong overlap of decreasing ground state and increasing excited state absorption bands. Spectral deconvolution using pseudo-Voigt profiles indicates a bleach entered at 408 nm with FWHM of 55 nm, and growth centered at 403 nm (FWHM of 65 nm).[32]

$$pyr–Zr^{IV}–O–Co^{II} \;\rightarrow\; pyr^{\;-}–Zr^{IV}–O–Co^{III}$$
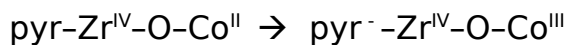
(3)

The oxidation of the Co donor center is confirmed by depletion of the Co^{II} d-d ligand field band between 500 and 650 nm (Figure 5B inset). Interestingly, the photo-induced electron transfer is exclusively observed for excitation wavelengths of 425 nm and shorter, i.e. for a much narrower range than the broad ZrOCo MMCT absorption that extends continuously from the UV to its onset around 600 nm, as shown in Figure 1D. This observation indicates that only assemblies in which pyridine interacts with the Zr center undergo electron transfer. The general acid-base interaction of the Zr center with adjacent pyridine may involve electron donation to the metal. Even minor

electron delocalization in the ground state would result in direct photoexcitation of a state with its pyr-Zr^{III}-Co-Co^{III} MMCT electronic character mixed partially with pyr^--Zr^{IV}-Co-Co^{III} character, opening an efficient path to full charge separation with the electron on pyridine that outcompetes back electron transfer within the ZrOCo unit. The rise time of the transient of 8 ns shown in Figure 5D is limited by the laser pulse width, as is expected for a MMCT initiated process featuring optical electron transfer from Co^{II} donor.

Since there is barely any decay of the transient absorption over hundreds of μs (Figure 5B), monitoring of the charge transfer process on the millisecond time scale by structure specific rapid-scan FT-IR spectroscopy was feasible, as shown in Figure 5C. The transient infrared bands in the 1700 – 1300 cm^{-1} region observed upon excitation of the pyr-ZrOCo units with a 405 nm light pulse (120 ms duration) agreed well with pyridine radical anion vibrational spectrum calculated by density functional theory, but not with the computed spectrum of the cation.[32] The single exponential decay of the radical and recovery of the ground state gave a lifetime of 220 $\pm$ 60 ms (room temperature) (Figure 5E). The very slow back electron transfer of the pyr^-–Zr^{IV}–O–Co^{III} charge-separated state is most likely due to spin crossover along the electron transfer path, with ultrafast flip of optically prepared high spin tetrahedral Co^{III} (S=1) to low spin Co^{III} (S=0) as a primary candidate, for which there are a number of precedents.[37-39] Despite the fact that the MMCT absorption of $TiOCo^{II}$ is stronger than that of $ZrOCo^{II}$ at any visible wavelength,[40] no transient infrared (Figure 5C, panel (c)) or optical signals

(Figure 5D) were detected for pyridine interacting with TiOCo units, consistent with the fact that transient Ti^{III} falls short by at least 0.5V of the reduction potential required for electron transfer to pyridine. Furthermore, no hole transfer from transient Co^{III} to pyridine is observed upon excitation of the MMCT state, demonstrating rectifying charge transfer behavior of this light absorber-pyridine system. This behavior is an important design aspect for charge transport pathways of hierarchically integrated artificial photosynthetic components. It will be critical for developing a 2-photon light absorber configuration by coupling of two heterobinuclear light absorber operating in tandem, each with energetically matched molecular wires that impose electron flow in the desired direction; efficient absorption of sunlight across its entire spectrum demands such a 2-photon light absorber configuration.[41,42]

B. Coupling of light absorber with catalysts for water oxidation or carbon dioxide reduction

For time-resolved optical monitoring of hole transfer from visible light absorber via wire embedded in the silica membrane to the Co_3O_4 catalyst core, ultrafast time resolution is needed because nanosecond absorption spectroscopy proved too slow for the detection of transient holes on PV3 molecules.[27,28] However, interpretation and analysis of ultrafast spectroscopic data requires a chromophore with established spectroscopic signature on fs and ps time scales, which is not yet available for heterobinuclear units (for

some units e.g. TiOMn, transient optical data have been obtained with nano and microsec time resolution).[43,44] Free-base porphyrin with positively charged ligands for strong adsorption on the (negatively polarized) silica particle surface (Figure 6A) has these properties including an appropriate redox potential for hole transfer to PV3 molecules.[33] Excitation of porphyrin adsorbed on a Co_3O_4-SiO_2 core-shell nanoparticle with embedded wire molecules into the Soret band with 430 nm laser pulses of 150 fs duration resulted in hole transfer to PV3 within a few hundred fs. This is manifested by the characteristic transient absorptions of PV3 radical cation in the range 500 to 650 nm and at 1130 nm, the latter shown in Figure 6B, accompanied by growth of reduced porphyrin radical anion with a peak at 695 nm (Figure 6C). The sub-ps arrival of the charge on the embedded wire is followed by decay on the tens of ps scale, shown in Figures 6B,C, and E under development of a bleach at 485 nm (Figure 6D), which marks arrival of holes on the Co_3O_4 catalyst.[33]

With hole transfer from light absorber to embedded wire molecules occurring within less than one ps, the overall rate of stepwise charge transfer to the catalyst is dictated by charge injection from the wire into the Co_3O_4 catalyst particle. The kinetic analysis for determining the rate constant for hole transfer from PV3 to Co_3O_4 is based on the diagram of Figure 7 whose energies were calculated by the Weller equation shown in the Figure. Computational fit of the decay curves of reduced free base porphyrin and PV3$^+$ radical cation of Figure 6E to a kinetic model that consists of

competition between forward hole transfer to Co_3O_4 (Co_3O_4-PV3$^+$-SiO$_2$•H$_2$P^{red}

→ Co_3O_4(h$^+$)-PV3-SiO$_2$•H$_2$P^{red}) and back charge transfer (Co_3O_4-PV3$^+$-

SiO$_2$•H$_2$P^{red} → Co_3O_4-PV3-SiO$_2$•H$_2$P) displayed in Figure 7 gave first order rate

constants k_2 = (3.9 ± 0.4) x 10^9 s^{-1} and k_1 = (1.6 ± 0.2) x 10^{10} s^{-1}. Hence, the

hole transfer time from silica embedded wire through the tripodal linker to

Co_3O_4 catalyst is 255 ps.[33] Combined with the laser pulse limited hole

transfer observed for the binuclear light absorber - embedded wire system,

this result implies that, in the case of MMCT systems, charge transfer across

the silica membrane via wires to the Co_3O_4 catalyst (Figure 1C) proceeds in 8

ns or faster. This rate is many orders of magnitude faster than reported so

far for charge transfer from a molecular light absorber to metal oxide

nanoparticle catalysts for water oxidation,[45] but similar to the ones observed

for hole injection into molecularly defined polyoxotungstate catalysts.[46] Fast

forward hole transfer is essential for outcompeting ever-present diversionary

charge transfer processes that degrade the efficiency of productive use of

separated charges.

We conclude that charge transfer between molecular light absorbers

like porphyrin and Co oxide water oxidation catalyst separated by an

ultrathin silica layer with embedded wire molecules, whose function is to

block interference of the incompatible catalytic environments, occurs within

250 ps. For the case of binuclear MMCT light absorbers, for which ultrafast

measurements are not yet available, an upper limit for the transfer time is 8

ns.

Chemical conversion of holes injected into Co_3O_4 proceeds by oxidation of surface Co^{III}-OH sites to Co^{IV}=O surface species, as discovered by transient ATR FT-IR measurements. Fast proton-coupled surface hopping of Co^{IV}=O species generated by arrival of consecutive holes leads to random encounters of these Co oxo species, which results in nucleophilic attack of H_2O to form peroxo and directly observed superoxo intermediates with small activation barriers.[23,47] Further encounter with hopping Co^{IV}=O releases O_2 and restarts the catalytic cycle. An increasing number of transient and steady-state infrared spectro(photo)electrochemical studies of water oxidation catalysis on first row transition metal surfaces indicate that these mechanistic features hold more generally.[48]

For Co oxide-silica core-shell nanotubes, heterobinuclear units anchored on the outside surface of the silica membrane drive the water oxidation catalysis on the Co_3O_4 inside surface (Figure 1). The ability of binuclear light absorbers to drive water oxidation at metal oxide nanoparticle catalysts was first demonstrated by spatially-directed coupling of the donor end to IrO_2 cluster. In the case of $TiOCr^{III}$, a $TiOCr^{V}$ precursor unit was exposed to an $Ir(acac)_3$ precursor (acac = acetylacetonate) that underwent redox reaction at the Cr center.[49] Mild calcination afforded Ir oxide nanocluster that were shown to evolve O_2 upon visible light excitation of $Ti^{IV}OCr^{III} \rightarrow Ti^{III}OCr^{IV}$ in aqueous solution. For $ZrOCo^{II}$ units, spatially defined coupling to IrO_2 nanocatalyst was achieved by photodeposition of $Ir(acac)_3$ utilizing the directionality of the MMCT chromophore; visible light induced

$Zr^{IV}OCo^{II} \rightarrow Zr^{III}OCo^{III}$ excitation resulted in redox linkage at the Co center followed by formation of an IrO_2 nanocluster upon calcination. The ZrOCo--IrO_2 unit anchored on silica surfaces was shown to oxidize vapor phase water. Because transient Zr^{III} produced upon MMCT excitation splits gas phase CO_2 to CO, the polynuclear ZrOCo--IrO_2 system affords photoreduction of vapor phase mixtures of CO_2 by H_2O to CO and O_2, i.e. closing of the photosynthetic cycle.[36]

At the acceptor site of excited binuclear units, chemical conversion of the electron by reduction of CO_2 to CO was not only observed for excited ZrOCo units,[36] but for other Zr containing binuclear units like ZrOCu.[50] Note that neither ZrOCu nor the ZrOCo requires the presence of a sacrificial donor. However, for artificial photosynthesis to become a viable renewable fuels technology, production of more energy dense hydrocarbon products than CO or formate is essential. Hence, our effort has focused on coupling of Cu-based nanoparticle catalysts at the Zr acceptor site; metallic Cu and cuprous oxide are unique catalytic materials in terms of the ability to reduce CO_2 to 4, 6 or more deeply reduced hydrocarbon products.[51] Exploiting the directionality of $Zr^{IV}OCo^{II} \rightarrow Zr^{III}OCo^{III}$ excitation for assembling a cuprous oxide nanocluster at the Zr end of the light absorber, illumination with visible light in the presence of Cu^{II} precursor with weakly held acetonitrile ligands, $Cu^{II}(NCCH_3)_4$, resulted in electron transfer from transient Zr^{III} to the precursor, generating Cu^{I} under loss of acetonitrile. Upon calcination, the ligand-deficient Cu center acts as nucleus for the formation of a copper cluster of

approx. 3 nm size (Figure 8A).[52] To explore the CO_2 half reaction, silica nanoparticles with anchored Cu_xO_y --$ZrOCo^{II}$ units were exposed to 1 atm of CO_2 gas in the presence of diethylamine as sacrificial donor. When illuminating the ZrOCo MMCT absorption, adsorbed bent CO_2 on the catalyst particle surface observed by FT-IR spectroscopy at 1682 cm^{-1} (^{13}C: 1656 cm^{-1}) converted to gas phase CO, as shown in Figure 8B,C. The yield was highest when reducing the surface Cu centers to the metallic state.[52] For catalytic transformation of CO_2 to more deeply reduced product, we are seeking to detect and structurally identify surface intermediates since such knowledge might guide ideas for catalyst modifications to bypass formation of CO or formate and steer the surface chemistry to higher carbon products. This effort has recently led to the discovery of carbon dioxide dimer radical anion as the one-electron reduction product of CO_2 at the Cu nanoparticle-aqueous interface.[53]

III. ALUMINA AND TITANIA NANOLAYERS FOR INTEGRATING MOLECULAR LIGHT ABSORBERS AND CATALYSTS

Ultrathin inert oxide layers prepared by ALD, such as silica, alumina or titania, have emerged as a new approach for the coupling organic or organometallic light absorbers and catalysts at photoanode or cathode surfaces for water splitting. Early reports of organic molecules anchored on electrode surfaces showed disaggregation upon casing into oxide layers,

thus reducing energy degrading pathways caused by interaction of neighboring light absorbers.[54-56] At the same time, the insulating oxide layer prevents undesired charge transfer or side reactions at the solid-aqueous interface, and drastically increases the durability of the attached light absorber by minimizing desorption from the electrode surface and chemical degradation during catalysis.[57-62] These phenomena are manifested in an increasing number of photoanode and cathode assemblies utilizing inert oxide nanolayers.

A. Transient optical spectroscopy

Transient optical absorption studies were conducted by Wasielewski and coworkers to explore the effect of Al_2O_3 nanolayers on a photoanode system consisting of perylene-3,4-dicarboximide (PMI) light absorber attached to TiO_2 nanoparticles and coupled to a molecular catalyst for water oxidation.[63] Anchored to the TiO_2 surface by carboxy groups, PMI was cast into Al_2O_3 layers of varying thickness in the range 1-3 nm (labeled nALD, n = number of ALD cycles applied, ~0.1 nm per cycle). Two types of molecular catalysts were subsequently immobilized randomly on the outer alumina surface, namely an oxo-bridged binuclear Ir complex or a mononuclear Ir complex with a phenylene linker as illustrated in the schematic of Figure 9A in right and left panel, respectively. Upon excitation of PMI with an ultrafast 495 nm photolysis pulse in the absence of an alumina layer, sub-ps electron transfer to TiO_2 (τ_2 in diagram Figure 9B) is accompanied by ground state bleach of

PMI centered at 520 nm and appearance of PMI excited state absorption at 680 nm (Figure 10A, top panel). Arrival of electrons in TiO_2 is further indicated by a broad maximum at 600 nm originating from Stark shift of the ground state PMI absorption to longer wavelengths induced by the local electric field caused by the electron transfer. Upon casting of 3 nm alumina (30ALD), electron injection into TiO_2 is slowed down by a modest factor of 1.6 as indicated by delayed growth of the 600 nm shoulder (Figure 10A, middle panel) and slower decrease of the 680 nm absorption of excited PMI at early times, shown in Figure 10B. According to the alumina thickness dependence shown of 5 ps time slices in the same Figure 10B, the retardation is primarily caused by the initial ~1 nm ALD layer. This phenomenon is attributed to passivation of TiO_2 surface traps by deposited alumina, blocking acceptor sites at the interface.

Comparison of the rate of the decay of excited PMI encased in 3 nm Al_2O_3 in the presence and absence of anchored binuclear Ir catalyst revealed a substantial acceleration of electron transfer to TiO_2 for samples with the IrIr catalyst as displayed in the kinetic traces of Figure 10C (hole transfer to the catalyst was inferred from the kinetic behavior of excited PMI chromophore because of very small extinction coefficients of IrIr or IrSil that did not permit the direct monitoring of these species). This is also manifested in the enhanced 600 nm maximum originating from the Stark-shifted PMI ground state absorption in the presence of the catalyst (Figure 10A, bottom panel). The spectral effects of the co-anchored binuclear Ir complex are attributed to

hole transfer from excited PMI to the catalyst (path τ_4 in Figure 9B) followed by electron injection from transient PMI radical anion so formed into the TiO_2 conduction band (path τ_6). The new charge transfer pathway opened up by hole injection into the catalyst is competitive with electron transfer from excited PMI to TiO_2 (τ_2) and therefore accelerates the decay of excited PMI and growth of Stark-shifted PMI. Hence, these results demonstrate that hole transfer from excited light absorber under electron injection into TiO_2 electrode takes place in the presence of the alumina layer, and that catalysts anchored randomly on an ultrathin inert oxide layer couple with embedded molecular light absorbers, allowing for charge transfer even in the absence of atomically defined linkage. Equally important, single wavelength 680 nm fits show increased charge separation lifetime between TiO_2 and catalyst (τ_7), demonstrating that the ALD layer slows down recombination of TiO_2 injected electron and oxidized catalyst, thereby increasing Faradaic efficiency of water oxidation. Enhanced photocurrent upon Al_2O_3 coating observed in parallel linear sweep voltammetry studies indicate that the benefits of ALD layers outweigh the slowdown of electron injection from the chromophore to TiO_2 observed in the ultrafast optical experiments. Hole transfer from excited PMI to the mononuclear Ir catalyst (Figure 9A, left panel) is not sufficiently efficient to result in an observable acceleration of the excited PMI decay (Figure 10C, green traces labeled IrSil). Yet, photoelectrochemical experiments show that the catalyst is indeed oxidized,

23

which implies that hole transfer to IrSil proceeds from transient PMI^+ radical cation formed by electron injection of excited PMI into TiO_2.[63]

B. Photoelectrochemical measurements

Casting of PMI light absorber into Al_2O_3 nanolayer upon anchoring on a NiO cathode was similarly beneficial for driving molecular hydrogen catalysts.[57] Since cobaloxime (CoL_2) or nickel phosphine (NiL_2, Figure 11A), both well-known proton reduction catalysts, were kept in solution thus requiring diffusion to the surface for the capture of electrons from excited or transient reduced PMI, this process escaped monitoring by ultrafast optical spectroscopy. Photocurrent versus time measurements in the presence of 0.5 nM Ni or Co catalyst under applied electrical bias of -0.4 V, shown in Figure 11B, gave tens of mA cm^{-2} for NiO/PMI cathodes with the light absorber fully encased in Al_2O_3 nanolayer. Monitoring of H_2 by gas chromatography under the same photoelectrochemical conditions showed H_2 generation with 100% Faradaic efficiency for Ni phosphine catalyst, which confirms efficient hole transfer from encapsulated light absorber to the catalyst. Important to note is the absence of capacitive peaks at the onset of each light pulse for experiments in the presence of a catalyst. This observation implies that electron transfer from transient PMI^- radical anion, formed upon hole injection into NiO anode, to the catalyst is fast for both the first and second electron, which holds for any alumina layer thickness up to and including complete encasement.[57]

Hole transfer from ultrathin oxide-embedded molecular light absorber to water oxidation catalyst has been explored for various configurations of these components on photoanodes by Meyer and coworkers. The constructs use SnO_2/TiO_2 or ITO/TiO_2 core shell particle films on an FTO electrode surface (ITO = indium tin oxide, FTO = fluorine tin oxide). The ultrathin TiO_2 shell affords retardation of back electron transfer from SnO_2 core to oxidized light absorber as directly demonstrated by ultrafast terahertz spectroscopy (a technique sensitive to changes in conductivity) and transient optical measurements by Mallouk and Schmuttenmaer.[58] The assembly shown in Figure 12A features triphenylamine light absorbers attached to the TiO_2 surface by a phosphonate group via thiophene linker and cast by ALD into an ultrathin TiO_2 shell. An efficient Ru bipyridyl water oxidation catalyst is anchored by a phosphonate group on the outside surface of the TiO_2 layer.[64] Illumination of the chromophore with 445 nm light (anode biased at 0.7 V vs. NHE) resulted in hole transfer to the Ru catalyst as indicated by several fold photocurrent enhancement compared to samples with no catalyst. Figure 12B shows the current density recorded upon 15 s illumination under simulated 1 sun emission in the presence (red curve) or absence of the catalyst (black curve) at 3 different light intensities, namely 7.8, 49, and 90 mW. The enhancement seen in the presence of the catalyst is actually larger than it appears in the plot because the data shown are not corrected for the loss of chromophore upon attachment of the catalyst. Oxygen produced by a similar assembly, namely triphenylamine light absorber featuring an

ethylene linker instead of the chemically more vulnerable thiophene bridge and cast into alumina instead of titania is shown in Figure 12C.[65] Evolved oxygen product at 0.4 V applied bias under 1 sun illumination is monitored electrochemically by O_2 reduction using a collector-generator dual working electrode.[64] The photoinduced current generated by charge transfer to the catalyst is represented by the solid red curve, while the collector current is shown in blue. Corresponding charge passed is indicated by dashed curves with values displayed on the right hand y-axis. Optimal charge transfer coupling was achieved for ALD alumina or titania nanolayer thickness in the range 0.6 to 1.0 nm. Thinner layers do not provide sufficient protection for the light absorber from desorption and too few anchoring sites for the phosphonate groups of the Ru catalyst, while thicker layers reduce the efficiency of hole transfer between light absorber and catalyst.

As expected, coupling of the molecular light absorber and water oxidation catalyst by a covalent bridge, in addition to metal oxide ALD casting of the assembly, gave an active photoanode as well. Figure 13A shows water oxidation at a photoanode featuring molecular Ru bis-bipyridyl light absorber and Ru catalyst covalently linked by a methylene bridge.[66] The photocatalytic water splitting performance (O_2 evolving photoanode shown in Figure 13A connected to a Pt cathode for H_2 evolution, 445 nm illumination) is of the same order of magnitude as for systems that do not have molecularly defined linkage between light absorber and catalyst. Therefore, the ALD attachment method introduces substantial simplification and

flexibility for the synthesis of hierarchical light absorber-catalyst assemblies without diminishing photocatalytic efficiency, yet dramatically improves durability. Similar advantages of ALD oxide layers for photoanode assemblies have been found for other types of molecular water oxidation catalysts, most recently for stabilizing highly active polyoxometalate catalysts.[67]

IV. FUTURE CHALLENGES

Emerging techniques for developing ultrathin inert oxide layers have opened up new approaches for coupling molecular light absorbers, catalysts, and assemblies of half reactions for overall water splitting, or for carbon dioxide reduction by water. Such layers effect dramatic improvements of the stability of surface attached molecules and allow for simplification and flexibility in the hierarchical assembly of the molecular and solid components to subsystems and complete systems. Physico-chemical characterization through monitoring of charge transfer by transient spectroscopy and photoelectrochemical techniques provides insights into pathways and rates, which prove critical for guiding synthetic improvements to achieve higher efficiency.

     To further develop the use of ultrathin oxide layers, a more detailed understanding of charge transfer, ion transport, and redox chemical processes at interfaces and in the interior of the layers is essential. Advanced spectroscopic techniques are required, and new ones may need to

be developed, for time and spatially resolved monitoring of these processes, which poses formidable technical challenges because of the buried solid-solid interface nature of these systems. Dynamic structure specific spectroscopies such as infrared on time scales from ultrafast to milliseconds need to be engaged for elucidating interfacial structural changes that accompany charge transfer, and for monitoring redox reactions driven by the charges.[68,69] Particularly insightful in the area of photoelectrodes will be time resolved spectroscopic monitoring under controlled applied potential, e.g. by infrared reflection absorption using the underlying metal electrode as reflecting surface or attenuated total reflection for nanolayer samples like those discussed in Sect. III (Figures 9 and 12). For such systems, the conducting surface allows control of the electrochemical potential of the oxide layer while temporal resolution of charge transport and catalytic processes can be achieved by pulsed visible light excitation of the molecular light absorbers. Alternatively, time resolution may be achieved by incremental jumps of the electrode potential using visible light excitation of the bandgap of an auxiliary semiconductor layer underneath an ultrathin metal electrode layer for inducing charge transfer or chemical transformations. Some aspects of such techniques have recently been employed for ultrafast or steady state infrared spectroelectrochemical studies of water oxidation mechanisms at metal oxide - aqueous interfaces.[70,71] Equally important is the probing of accompanying electronic structure dynamics of metal centers of light absorbers, catalysts, or metal

oxide interfaces by time-resolved X-ray spectroscopy including the ultrafast time regime accessible by synchrotron and X-ray free electron laser sources where similar methods for triggering of processes as outlined for optical and vibrational studies can be employed.[72] Surface sensitive X-ray methods such as ambient pressure X-ray photoelectron spectroscopy are particularly suitable for elucidating ultrathin oxide interfacial structures and dynamics.[73,74]

An exciting new direction opened up by ultrathin oxide layers is the development of nanoscale artificial photosystems that integrate robust inorganic photocatalysts for water oxidation and microbial cells for the reduction of carbon dioxide to energy dense fuel molecules. Microbes offer low energy pathways for converting CO_2 to complex organics at product selectivity currently beyond reach for abiotic catalysis. Coupling of inorganic semiconductor based H_2O splitting photocatalysts with CO_2 reducing microbes generating C_2 molecules such as acetate or higher carbon products like isopropanol was recently demonstrated for macroscale integrated systems by the groups of Nocera and Yang.[75-77] To function properly, macroscale separation of the incompatible abiotic and biotic reaction environments is currently required to prevent corrosion, poisoning, and fouling. Nanoscale integration would minimize or even avoid these damaging processes and provide the efficiency advantages of coupling on the shortest possible length scale already pointed out for purely abiotic photosystems. The feasibility of 2 nm thick silica membranes with embedded electron

conducting molecular wires energetically matched with the potential of electron exporting bacteria on one side and SnO_2 catalyst on the opposite side has recently been demonstrated.[30] This enables separation of biotic and abiotic environments on the nanoscale, thus opening up the exploration of nanoscale artificial photosystems that couple inorganic visible light water oxidation catalysts with microbial organisms for converting CO_2 and H_2O to energy dense fuels.

A further unique advantage of nanoscale integration of incompatible photocatalytic environments enabled by ultrathin oxide membranes is the immense design space available for scale up because of the large variety of nanostructures, allowing great flexibility in tailoring the morphology of the integrated nanosystems to the photocatalytic function at hand. Nanomaterials synthesis allows for an enormous range of macroscale geometries to choose from, which in turn enables optimization of the efficiency of photocatalytic systems, e.g. for specific fuel targets. Elucidation of mechanisms and efficiency of charge transport and chemical transformations at each step of systems assembly from nanoscale units to macroscale will be the key for guiding designs and optimizing photocatalytic performance.

ACKNOWLEDGMENTS

References

[1] R. W. Johnson, A. Hultqvist, and S. F. Bent, Mater. Today **17**, 236-246 (2014).

[2] Y. W. Chen, J. D. Prange, S. Duehnen, Y. Park, M. Gunji, C. E. D. Chidsey, and P. C. McIntyre, Nature Mater. **10**, 539-544 (2011).

[3] A. G. Scheuermann, J. P. Lawrence, K. W. Kemp, T. Ito, A. Walsh, C. E. D. Chidsey, P. K. Hurley, and P. C. McIntyre, Nature Mater. **15**, 99-106 (2016).

[4] M. F. Lichterman, A. I. Carim, M. T. McDowell, S. Hu, H. B. Gray, B. S. Brunschwig, and N. S. Lewis, Energy Environ. Sci. **7**, 3334-3337 (2014).

[5] M. T. McDowell, M. F. Lichterman, J. M. Spurgeon, H. Shu, I. D. Sharp, B. S. Brunschwig, and N. S. Lewis, J. Phys. Chem. C **118**, 19618-19624 (2014).

[6] S. Hu, M. R. Shaner, J. A. Beardslee, M. Lichterman, B. S. Brunschwig, and N. S. Lewis, Science **344**, 1005-1009 (2014).

[7] E. Verlage, S. Hu, R. Liu, R. J. R. Jones, K. Sun, C. Xiang, N. S. Lewis, and H. A. Atwater, Energy Environ. Sci. **8**, 3166-3172 (2015).

[8] C. Zachaus, F. F. Abdi, L. M. Peter, and R. van de Krol, Chem. Sci. **8**, 3712-3719 (2017).

[9] K. Sun, F. H. Saadi, M. F. Lichterman, W. G. Hale, H. P. Wang, X. Zhou, N. T. Plymale, S. T. Omelchenko, J. H. He, K. M. Papadantonakis, B. S. Brunschwig, and N. S. Lewis, Proc. Natl. Acad. Sci. U.S.A. **112**, 3612-3617 (2015).

[10] K. Maeda, K. Teramura, D. Lu, N. Saito, Y. Inoue, and K. Domen, Angew. Chem. Int. Ed. **45**, 7806-7809 (2006).

[11]   M. Yoshida, K. Takanabe, K. Maeda, A. Ishikawa, J. Kubota, Y. Sakata, Y. Ikezawa, and K. Domen, J. Phys. Chem. C **113**, 10151-10157 (2009).

[12]   M. Yoshida, K. Maeda, D. Lu, J. Kubota, and K. Domen, J. Phys. Chem. C **117**, 14000-14006 (2013).

[13]   A. T. Garcia-Esparza, T. Shinagawa, S. Ould-Chikh, M. Qureshi, X. Peng, N. Wei, D. H. Anjum, A. Clo, T. C. Weng, D. Nordlund, D. Sokaras, J. Kubota, K. Domen, and K. Takanabe, Angew. Chem. Int. Ed. **56**, 5780-5784 (2017).

[14]   C. W. Moore, J. Li, and P. A. Kohl, J. Electrochem. Soc. **152**, A1606-A1612 (2005).

[15]   Y. Aoki, E. Muto, A. Nakao, and T. Kunitake, Adv. Mater. **20**, 4387-4393 (2008).

[16]   N. Y. Labrador, E. L. Songcuan, C. De Silva, H. Chen, S. J. Kurdziel, R. K. Ramachandran, C. Detavernier, and D. V. Esposito, ACS Catal. **8**, 1767-1778 (2018).

[17]   G. Yuan, A. Agiral, N. Pellet, W. Kim, and H. Frei, Faraday Discuss. **176**, 233-249 (2014).

[18]   T. Hisatomi and K. Domen, Curr. Opin. Electrochem. **2**, 148-154 (2017).

[19]   D. V. Esposito, ACS Catal. **8**, 457-465 (2018).

[20] N. A. Campbell, J. B. Reece, M. R. Taylor, and E. J. Simon, Biology: Concepts & Connections, 5th ed. (Educational Pearson, New York, 2006).

[21]   R. E. Blankenship, D. M. Tiede, J. Barber, G. W. Brudvig, G. R. Fleming, M. Ghirardi, M. R. Gunner, W. Junge, D. M. Kramer, A. Melis, T. A. Moore, C. C. Moser, D. G. Nocera, A. J. Nozik, D. R. Ort, W. W. Parson, R. C. Prince, and R. T. Sayre, Science **332**, 805-809 (2011).

[22]   E. Edri, S. Aloni, and H. Frei, ACS Nano **12**, 533-541 (2018).

[23]   M. Zhang, M. de Respinis, and H. Frei, Nature Chem. **6**, 362-367 (2014).

[24]   W. Kim, B. A. McClure, E. Edri, and H. Frei, Chem. Soc. Rev. **45**, 3221-3243 (2016).

[25]   W. Kim, E. Edri, and H. Frei, Acc. Chem. Res. **49**, 1634-1645 (2016).

[26]   M. L. Macnaughtan, H. S. Soo, and H. Frei, J. Phys. Chem. C **118**, 7874-7885 (2014).

[27]   H. S. Soo, A. Agiral, A. Bachmeier, and H. Frei, J. Am. Chem. Soc. **134**, 17104-17116 (2012).

[28]   A. Agiral, H. S. Soo, and H. Frei, Chem. Mater. **25**, 2264-2273 (2013).

[29]   E. Edri and H. Frei, J. Phys. Chem. C **119**, 28326-28334 (2015).

[30]   J. A. Cornejo, H. Sheng, E. Edri, C. A. Ajo-Franklin, and H. Frei, Nature Commun. **9**: 2263 (2018).

[31]   G. Katsoukis, and H. Frei, ACS Appl. Mater. Interfaces **10**, 31422-31432 (2018).

[32]   A. D. Hill, G. Katsoukis, and H. Frei, J. Phys. Chem. C **122**, 20176-20185 (2018).

[33]   E. Edri, J. K. Cooper, I. D. Sharp, D. M. Guldi, and H. Frei, J. Am. Chem. Soc. **139**, 5458-5466 (2017).

[34] N. J. Curtis, G. A. Lawrance, and A. M. Sargeson, Aust. J. Chem. **36**, 1327-1339 (1983).

[35] W. B. Davis, M. A. Ratner, and M. R. Wasielewski, Chem. Phys. **281**, 333-346 (2002).

[36] W. Kim, G. Yuan, B. A. McClure, and H. Frei, J. Am. Chem. Soc. **136**, 11034-11042 (2014).

[37]   W. Zhang and K. J. Gaffney, Acc. Chem. Res. **48**, 1140-1148 (2015).

[38]   M. Kabir and K. J. Van Vliet, Phys. Rev. B **85**, 054431 (2012).

[39]   O. Sato, T. Iyoda, A. Fujishima, and K. Hashimoto, Science **272**, 704 (1996).

[40]   H. Han and H. Frei, Microporous Mesoporous Mater. **103**, 265-272 (2007).

[41] M. C. Hanna and A. J. Nozik, J. Appl. Phys. **100**, 074510 (2006).

[42] J. R. Bolton, S. J. Strickler, and J. S. Connolly, Nature **316**, 495 (1985).

[43]   T. Cuk, W. W. Weare, and H. Frei, J. Phys. Chem. C **114**, 9167-9172 (2010).

[44]   B. A. McClure and H. Frei, J. Phys. Chem. C **118**, 11601-11611 (2014).

[45] W. J. Youngblood, H. A. Lee, Y. Kobayashi, E. Hernadez-Pagan, P. G. Hoertz, T. A. Moore, A. L. Moore, D. Gust, and T. E. Mallouk, J. Am. Chem. Soc. **131**, 926-927 (2009).

[46]   X. Xiang, J. Fielden, W. Rodriguez-Cordoba, Z. Huang, N. Zhang, D. G. Luo, D. G. Musaev, T. Lian, and C. L. Hill, J. Phys. Chem. C **117**, 918-926 (2013).

[47]   H. H. Pham, M. J. Cheng, H. Frei, L. W. Wang, ACS Catal. **6**, 5610-5617 (2016).

[48]   M. Zhang and H. Frei, Annu. Rev. Phys. Chem. **68**, 209-231 (2017).

[49]   H. Han and H. Frei, J. Phys. Chem. C **112**, 16156-16159 (2008).

[50]   W. Lin and H. Frei, J. Am. Chem. Soc. **127**, 1610-1611 (2005).

[51]   Y. Hori, in Modern Aspects of Electrochemistry, Vol 42 (Springer, New York, 2008); pp. 89-189.

[52]   W. Kim and H. Frei, ACS Catal. **5**, 5627-5635 (2015).

[53]   H. Sheng, M. H. Oh, W. T. Osowiecki, W. Kim, A. P. Alivisatos, and H. Frei, J. Am. Chem. Soc. **140**, 4363-4371 (2018).

[54]   H. J. Son, X. Wang, C. Prasittichai, N. C. Jeong, T. Aaltonen, R. G. Gordon, and J. T. Hupp, J. Am. Chem. Soc. **134**, 9537-9540 (2012).

[55]   D. Hausmann, J. Becker, W. Wang, and R. G. Gordon, Science **298**, 402-406 (2002).

[56]   L. J. Antila, M. J. Heikkila, V. Makinen, N. Humalamaki, M. Laitinen, V. Linko, P. Jalkanen, J. Toppari, V. Aumanen, M. Kemell, P. Myllyperio, K. Honkala, H. Hakkinen, M. Leskela, J. E. I. Korppi-Tommola, J. Phys. Chem. C **115**, 16720-16729 (2011).

[57]   R. J. Kamire, M. B. Majewski, W. L. Hoffeditz, B. T. Phelan, O. K. Farha, J. T. Hupp, and M. R. Wasielewski, Chem. Sci. **8**, 541-549 (2017).

[58]   J. R. Swierk, N. S. McCool, C. T. Nemes, T. E. Mallouk, and C. A. Schmuttenmaer, J. Phys. Chem. C **120**, 5940-5948 (2016).

[59]   A. K. Vannucci, L. Alibabaei, M. D. Losego, J. J. Concepcion, B. Kalanyan, G. N. Parson, and T. J. Meyer, Proc. Natl. Acad. Sci. USA **110**, 20918-20922 (2013).

[60]   M. K. Brennaman, R. J. Dillon, L. Alibabaei, M. K. Gish, C. J. Dares, D. L. Ashford, R. L. House, G. J. Meyer, J. M. Papanikolas, and T. J. Meyer, J. Am. Chem. Soc. **138**, 13085-13102 (2016).

[61]   M. D. Losego and K. Hanson, Nano Energy **2**, 1067-1069 (2013).

[62]   K. Hanson, M. D. Losego, B. Kalanyan, D. L. Ashford, G. N. Parsons, and T. J. Meyer, Chem. Mater. **25**, 3-5 (2013).

[63]   R. J. Kamire, K. L Materna, W. L. Hoffeditz, B. R. Phelan, J. M. Thompson, O. K. Fahra, J. T. Hupp, G. W. Brudvig, and M. R. Wasielewski, J. Phys. Chem. C **121**, 3752-3764 (2017).

[64]   L. Alibabaei, R. J. Dillon, C. E. Reilly, M. K. Brennaman, K. R. Wee, S. L. Marquard, J. M. Papanikolas, and T. J. Meyer, ACS Appl. Mater. Interfaces **9**, 39018-39026 (2017).

[65]   M. S. Eberhart, D. Wang, R. N. Sampaio, S. L. Marquard, B. Shan, M. K. Brennaman, G. J. Meyer, C. Dares, and T. J. Meyer, J. Am. Chem. Soc. **139**, 16248-16255 (2017).

[66]   L. Alibabaei, B. D. Sherman, M. R. Norris, M. K. Brennaman, and T. J. Meyer, Proc. Natl. Acad. Sci. U.S.A. **112**, 5899-5902 (2015).

[67]   S. M. Lauinger, B. D. Piercy, W. Li, Q. Yin, D. L. Collins-Wildman, E. N. Glass, M. D. Losego, D. Wang, Y. V. Geletii, and C. L. Hill, ACS Appl. Mater. Interfaces **9**, 35048-35056 (2017).

[68]   J. Song, A. Ge, B. Piercy, M. D. Losego, and T. Lian, Chem. Phys. **512**, 68-74 (2018).

[69]   H. Sheng and H. Frei, J. Am. Chem. Soc. **138**, 9959-9967 (2016).

[70]   D. M. Herlihy, M. M. Waegele, X. Chen, C. D. Pemmaraju, D. Prendergast, and T. Cuk, Nature Chem. **8**, 549-555 (2016).

[71]   O. Zandi and T. W. Hamann, Nature Chem. **8**, 778-783 (2016).

[72]   X-ray Free Electron Lasers, edited by U. Bergmann, V. K. Yachandra, and J. Yano, eds., Energy Environ. Series (Royal Society of Chemistry: Cambridge, 2018).

[73]   M. Favaro, H. Xiao, T. Cheng, W. A. Goddard, J. Yano, and E. J. Crumlin, Proc. Natl. Acad. Sci. U.S.A. **114**, 6706-6711 (2017).

[74]   S. Nemsak, A. Shavorskiy, O. Karslioglu, I. Zegkinoglou, A. Rattanachata, C. S. Conlon, A. Keqi, P. K. Greene, E. C. Burks, F. Salmassi, E. M. Gullikson, S. H. Yang, K. Liu, H. Bluhm, and C. S. Fadley, Nature. Commun. **5**:5441 (2014).

[75]   J. P. Torella, C. J. Gagliardi, J. S. Chen, D. K. Bediako, B. Colon, J. C. Way, P. A. Silver, and D. G. Nocera, Proc. Natl. Acad. Sci. USA **112**, 2337-2342 (2015).

[76]   C. Liu, B. C. Colon, M. Ziesack, P. A. Silver, and D. G. Nocera, Science **352**, 1210-1213 (2016).

[77]   C. Liu, J. J. Gallagher, K. K. Sakimoto, E. M. Nichols, C. J. Chang, M. C. Chang, and P. D. Yang, Nano Lett. **15**, 3634-3639 (2015).
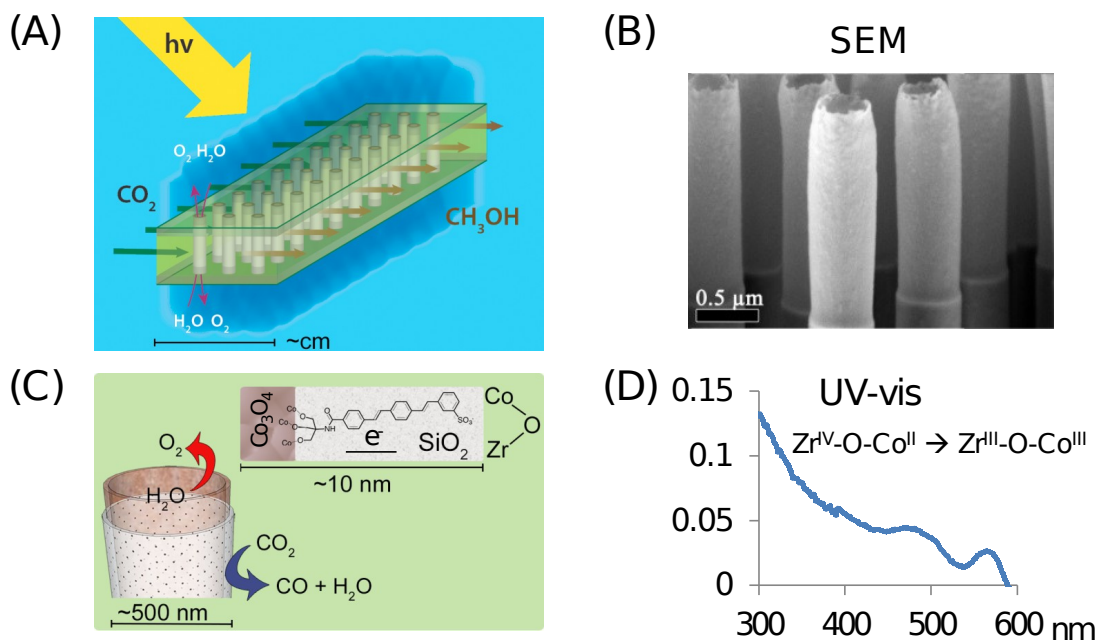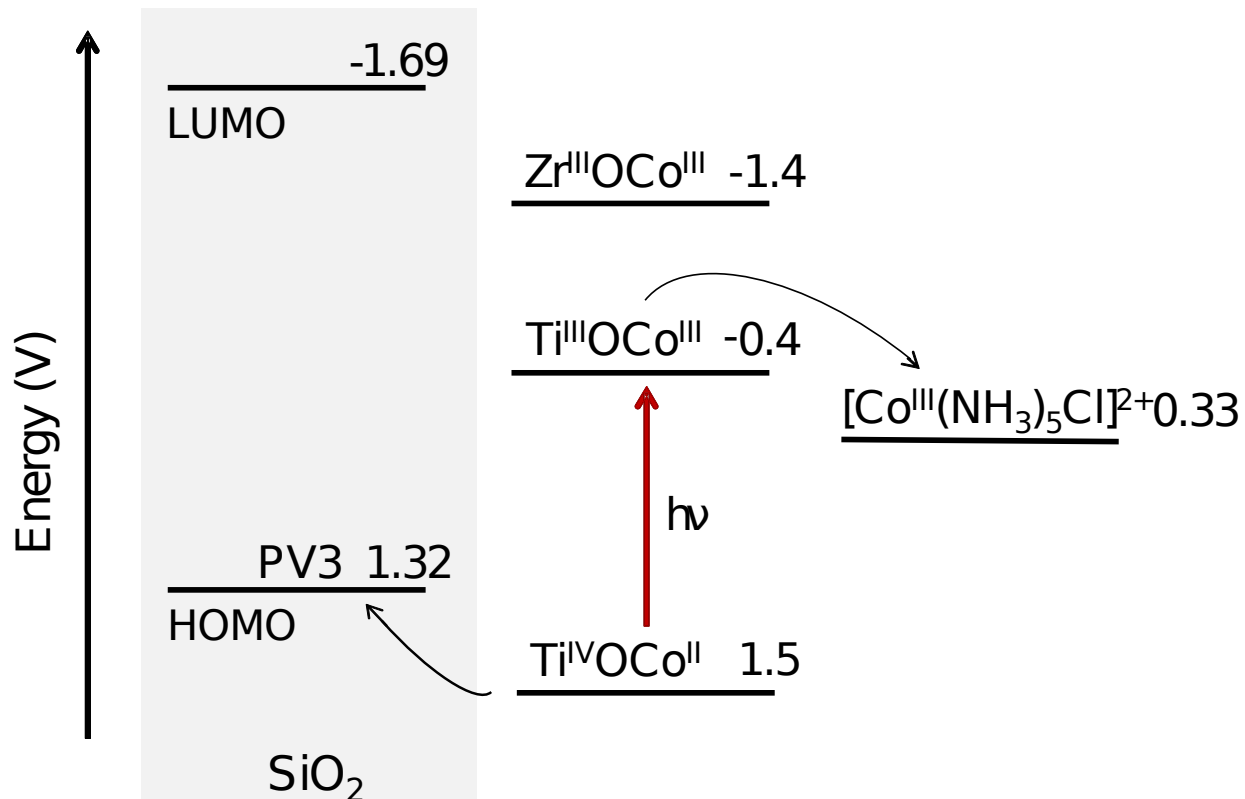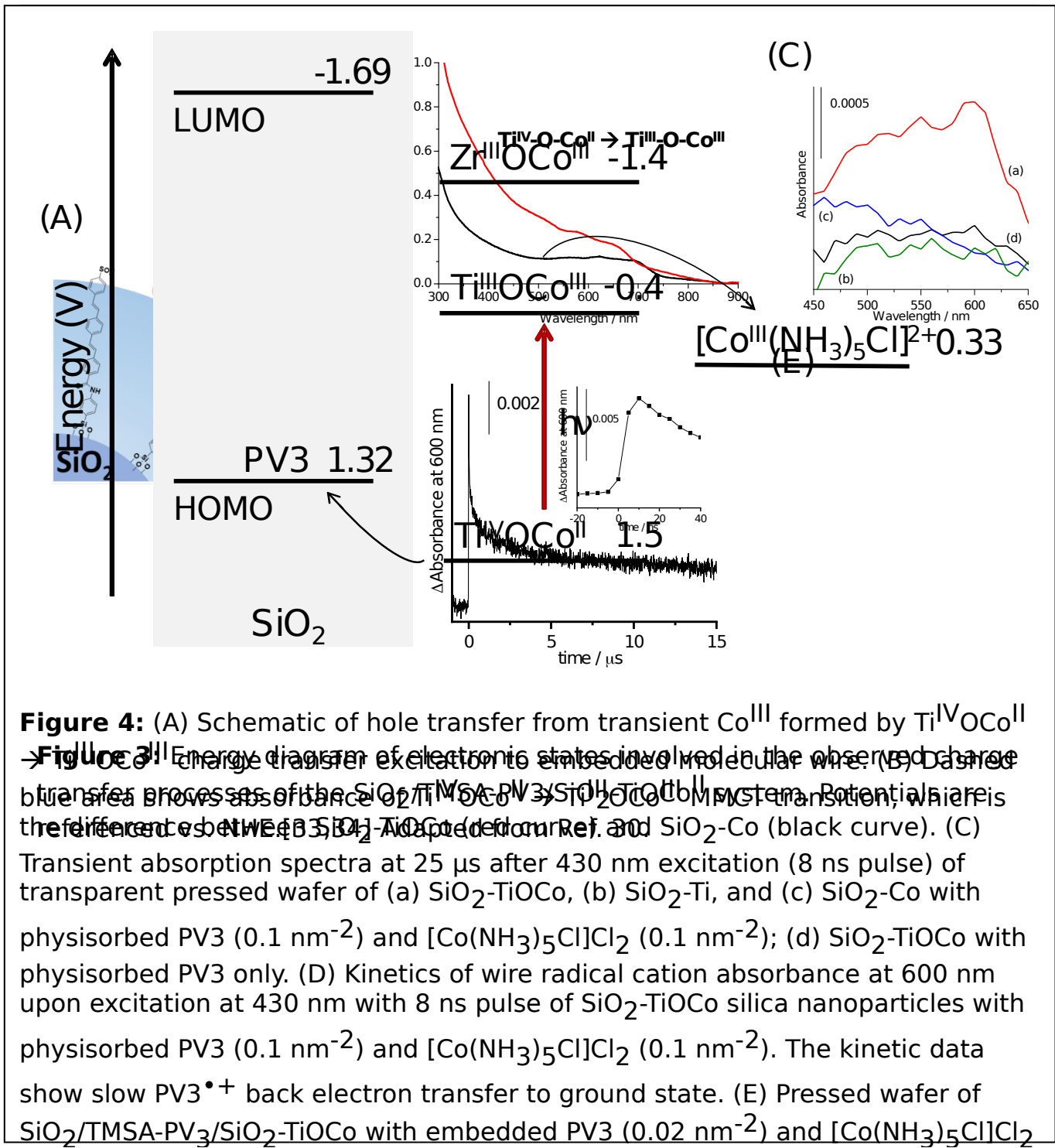
Figure 1: (A) Cobalt oxide-silica core-shell nanotube array design for artificial photosynthesis. (B) SEM image of a section of the array. (C) Each nanotube consists of a 5−10 nm thick inner Co_3O_4 tube (brown) where water oxidation takes place on the inside surface. The tube is surrounded by a 2-3 nm thick dense phase silica shell (gray) that acts as a proton conducting, O_2 impermeable membrane separating the water oxidation catalysis on the inside from charge transfer light absorber and CO_2 reduction sites on the outside. Control of electron transport across the silica membrane is accomplished by molecular wires in the silica (inset: expanded view of wall). The spaces of O_2 evolution and fuel generation do not intersect. Reproduced with permission from ACS Nano 12, 533 (2018). Copyright 2018 American Chemical Society. (D) UV-vis spectrum of ZrOCo MMCT light absorber.
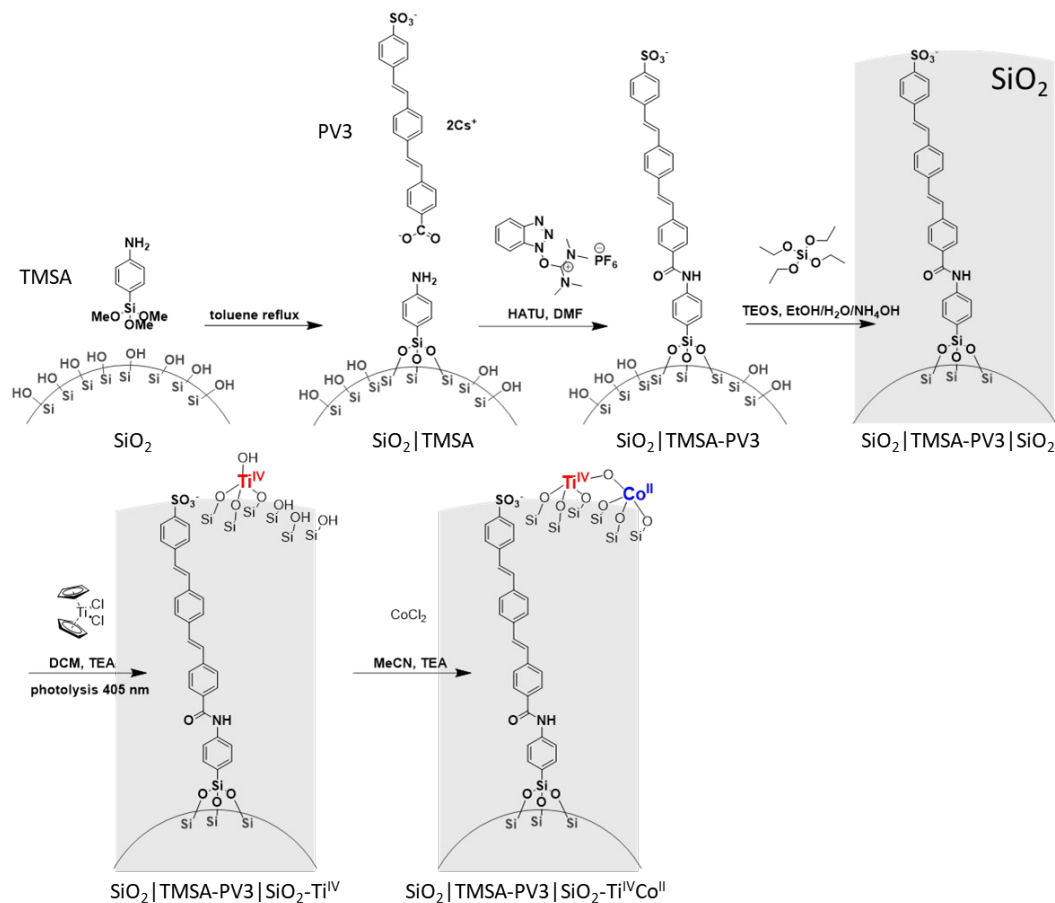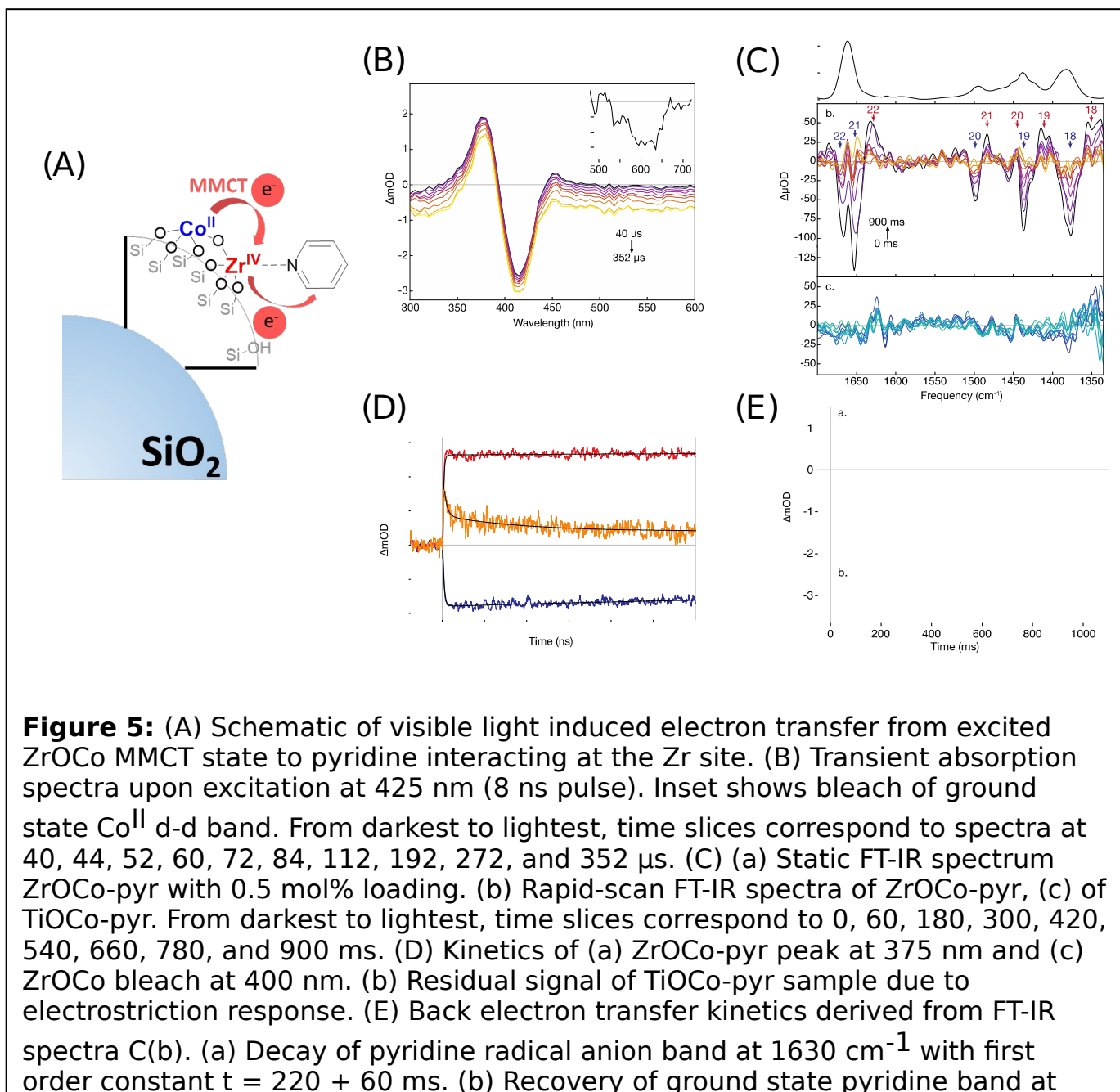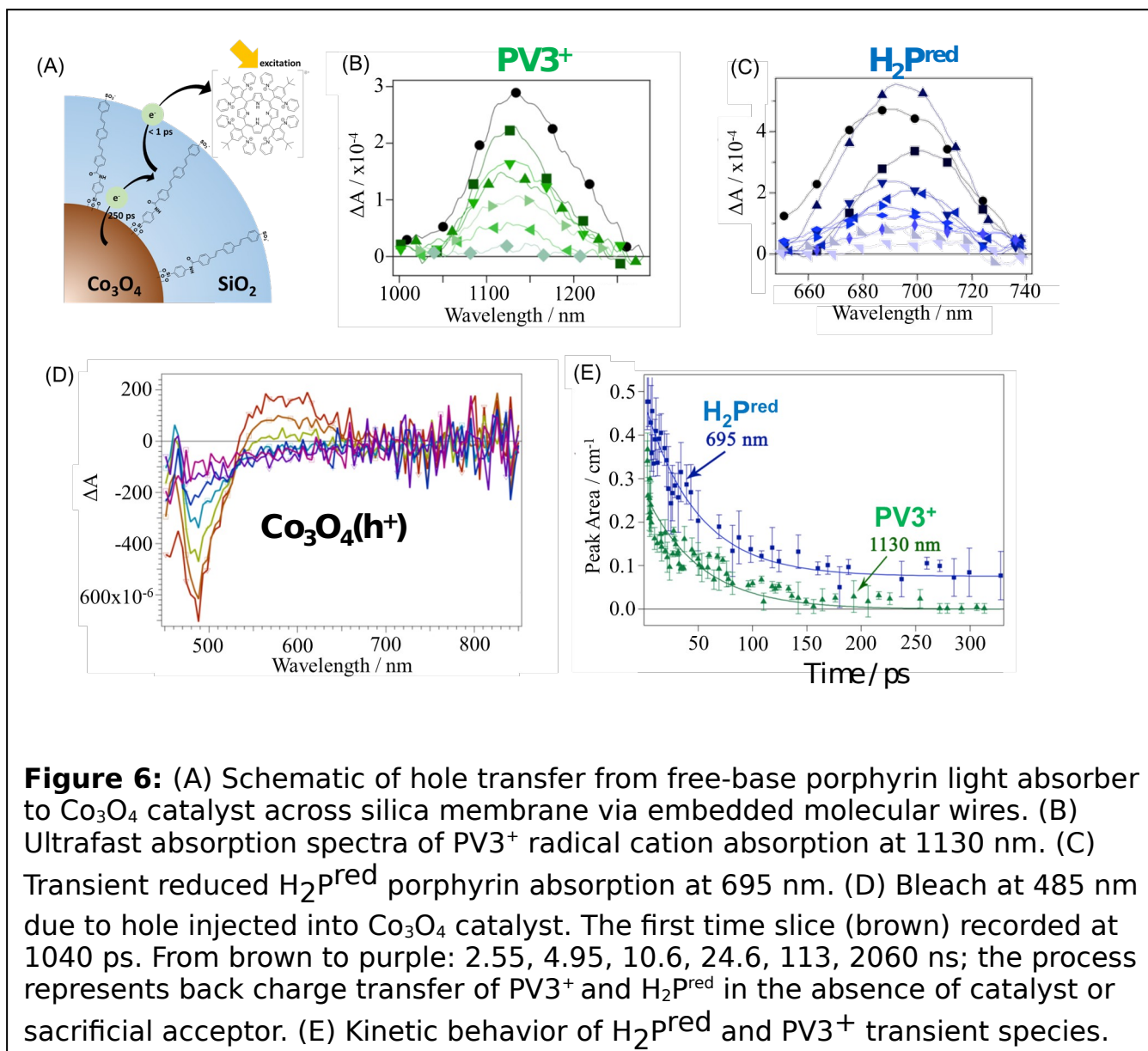
Figure 2: Stepwise assembly of molecular wires vertically aligned on silica nanoparticles cast into an ultrathin silica layer, and surface attachment of $Ti^{IV}OCo^{II}$ light absorber. TMSA = 4-(trimethoxysilyl) aniline, HATU = O-(7-Azabenzotriazol-1-yl)-N,N,N′,N′-tetramethyluronium-hexafluorphosphate, TEOS = tetraethoxy silane, DCM = dichloromethane, TEA = trimethylamine. Reproduced with permission from ACS Appl. Mater. Interfaces **10**, 31422 (2018). Copyright 2018 American Chemical
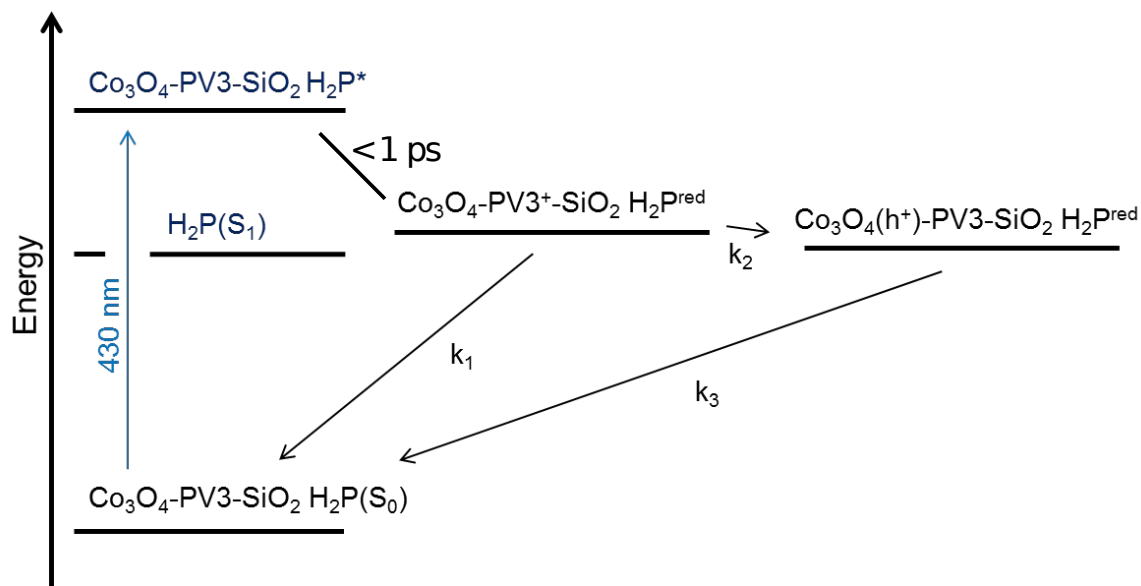
Figure 3: Energy diagram of electronic states involved in the observed charge transfer processes of the SiO_2/TMSA-PV3/SiO_2-TiOCo^{II} system. Potentials are referenced vs. NHE.[33,34] Reproduced with permission from ACS Appl. Mater. Interfaces **10**, 31422 (2018). Copyright 2018 American Chemical Society.

Figure 4: (A) Schematic of hole transfer from transient Co^{III} formed by Ti^{IV}OCo^{II} → Ti^{III}OCo^{III} charge transfer excitation to embedded molecular wire. (B) Dashed blue area shows absorbance of Ti^{IV}OCo^{II} → Ti^{III}OCo^{III} MGT transition, which is the difference between SiO$_2$-TiOCo (red curve) and SiO$_2$-Co (black curve). (C) Transient absorption spectra at 25 μs after 430 nm excitation (8 ns pulse) of transparent pressed wafer of (a) SiO$_2$-TiOCo, (b) SiO$_2$-Ti, and (c) SiO$_2$-Co with physisorbed PV3 (0.1 nm^{-2}) and [Co(NH$_3$)$_5$Cl]Cl$_2$ (0.1 nm^{-2}); (d) SiO$_2$-TiOCo with physisorbed PV3 only. (D) Kinetics of wire radical cation absorbance at 600 nm upon excitation at 430 nm with 8 ns pulse of SiO$_2$-TiOCo silica nanoparticles with physisorbed PV3 (0.1 nm^{-2}) and [Co(NH$_3$)$_5$Cl]Cl$_2$ (0.1 nm^{-2}). The kinetic data show slow PV3$^{\bullet +}$ back electron transfer to ground state. (E) Pressed wafer of SiO$_2$/TMSA-PV$_3$/SiO$_2$-TiOCo with embedded PV3 (0.02 nm^{-2}) and [Co(NH$_3$)$_5$Cl]Cl$_2$

43

Figure 5: (A) Schematic of visible light induced electron transfer from excited ZrOCo MMCT state to pyridine interacting at the Zr site. (B) Transient absorption spectra upon excitation at 425 nm (8 ns pulse). Inset shows bleach of ground state Co^{II} d-d band. From darkest to lightest, time slices correspond to spectra at 40, 44, 52, 60, 72, 84, 112, 192, 272, and 352 μs. (C) (a) Static FT-IR spectrum ZrOCo-pyr with 0.5 mol% loading. (b) Rapid-scan FT-IR spectra of ZrOCo-pyr, (c) of TiOCo-pyr. From darkest to lightest, time slices correspond to 0, 60, 180, 300, 420, 540, 660, 780, and 900 ms. (D) Kinetics of (a) ZrOCo-pyr peak at 375 nm and (c) ZrOCo bleach at 400 nm. (b) Residual signal of TiOCo-pyr sample due to electrostriction response. (E) Back electron transfer kinetics derived from FT-IR spectra C(b). (a) Decay of pyridine radical anion band at 1630 cm^{-1} with first order constant t = 220 $\pm$ 60 ms. (b) Recovery of ground state pyridine band at

Figure 6: (A) Schematic of hole transfer from free-base porphyrin light absorber to Co_3O_4 catalyst across silica membrane via embedded molecular wires. (B) Ultrafast absorption spectra of $PV3^+$ radical cation absorption at 1130 nm. (C) Transient reduced H_2P^{red} porphyrin absorption at 695 nm. (D) Bleach at 485 nm due to hole injected into Co_3O_4 catalyst. The first time slice (brown) recorded at 1040 ps. From brown to purple: 2.55, 4.95, 10.6, 24.6, 113, 2060 ns; the process represents back charge transfer of $PV3^+$ and H_2P^{red} in the absence of catalyst or sacrificial acceptor. (E) Kinetic behavior of H_2P^{red} and $PV3^+$ transient species.

$$\Delta G_{el}(kcal \cdot mol^{-1}) = 23.06 \cdot \left[\varepsilon^0(PV3^+/PV3) - \varepsilon^0\left(H_2P/H_2P^{red}\right)\right] - w_{el}\left(PV3^+/H_2P^{red}\right)$$
$$+ w_{el}(PV3/H_2P) - \Delta G_{00}$$

Figure 7: Energy diagram of electronic states involved in the observed charge transfer processes of the Co_3O_4- PV3$-SiO_2 \cdot H_2P$ system. The Weller equation used for calculating energies is shown. Reproduced with permission from J. Am. Chem. Soc. **139**, 5458 (2017). Copyright 2017 American Chemical Society.
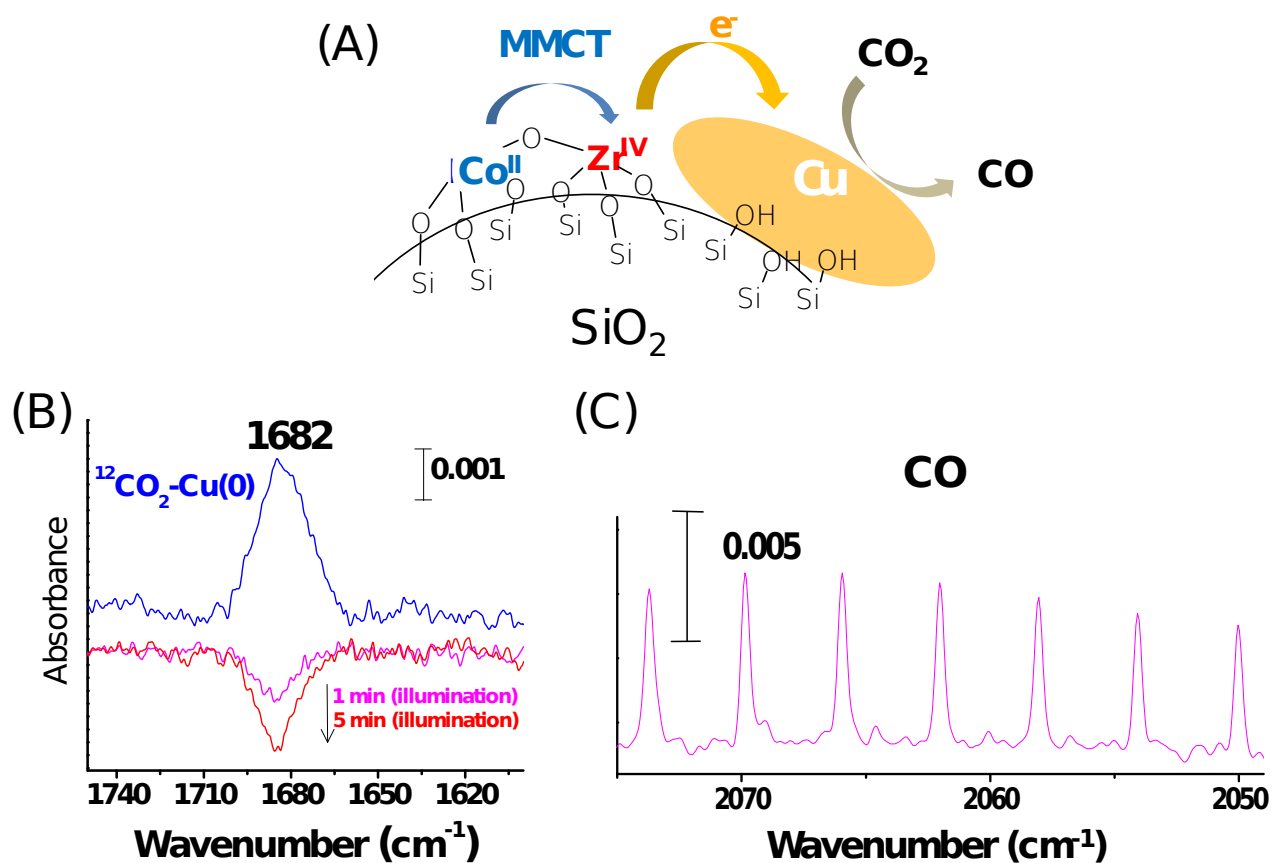
Figure 8: (A) Hierarchical assembly of an oxo-bridged binuclear ZrOCo[II] light absorber unit coupled to a cuprous oxide nanocluster catalyst for CO_2 reduction on mesoporous silica SBA-15 support. ZrOCo[II] unit functions as light absorber, donating electrons to the Cu_xO_y catalyst on whose surface CO_2 is reduced. (B) FT-IR spectra of $^{12}CO_2$ adsorbed on Cu_xO_y-ZrOCo SBA-15 after carbon dioxide loading (760 Torr) and subsequent evacuation (blue trace). Additional spectral traces show depletion of the band upon 355 nm irradiation for 1 min (pink), and 5 min (red) in the presence of 0.5 Torr diethylamine sacrificial donor. (C) Difference FT-IR spectrum of gas phase ^{13}CO growth upon 355 nm irradiation of Cu_xO_y-ZrOCo[II] SBA-15 for 5 h in the presence of 760 Torr $^{13}CO_2$ and 0.5 Torr
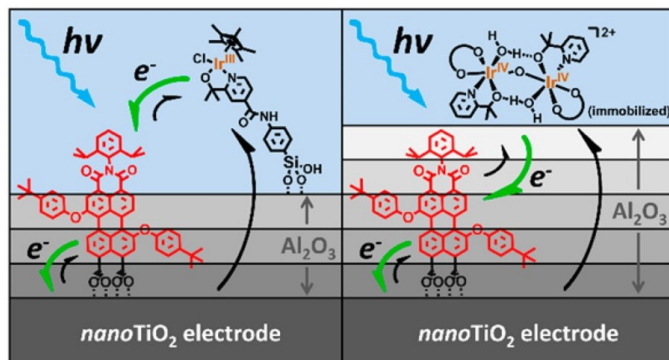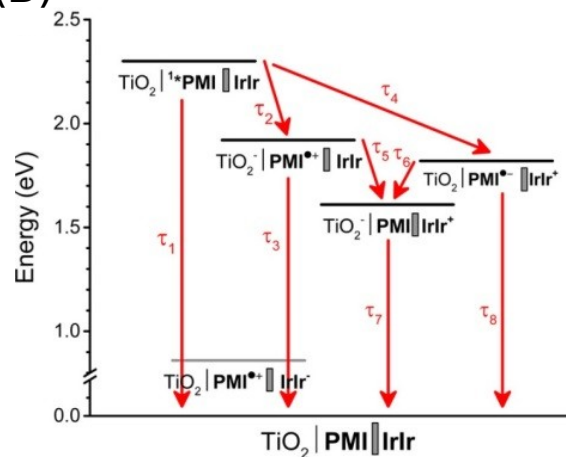
Figure 9: (A) Schematic of perylene-3,4-dicarboximide (PMI) light absorber (red) on TiO$_2$ photoanode encased by Al$_2$O$_3$ nanolayer deposited by ALD. Two different types of Ir based organometallic catalysts for water oxidation (black) labeled IrSil (left) and IrIr (right) are anchored on the outer alumina surface. (B) Energy level diagram for TiO$_2$/PMI/Al$_2$O$_3$/IrIr, showing hole transfer pathways from excited PMI chromophore to anchored catalyst. Reproduced with permission from J. Phys. Chem. C **121**, 3752 (2017). Copyright 2017 American Chemical Society.
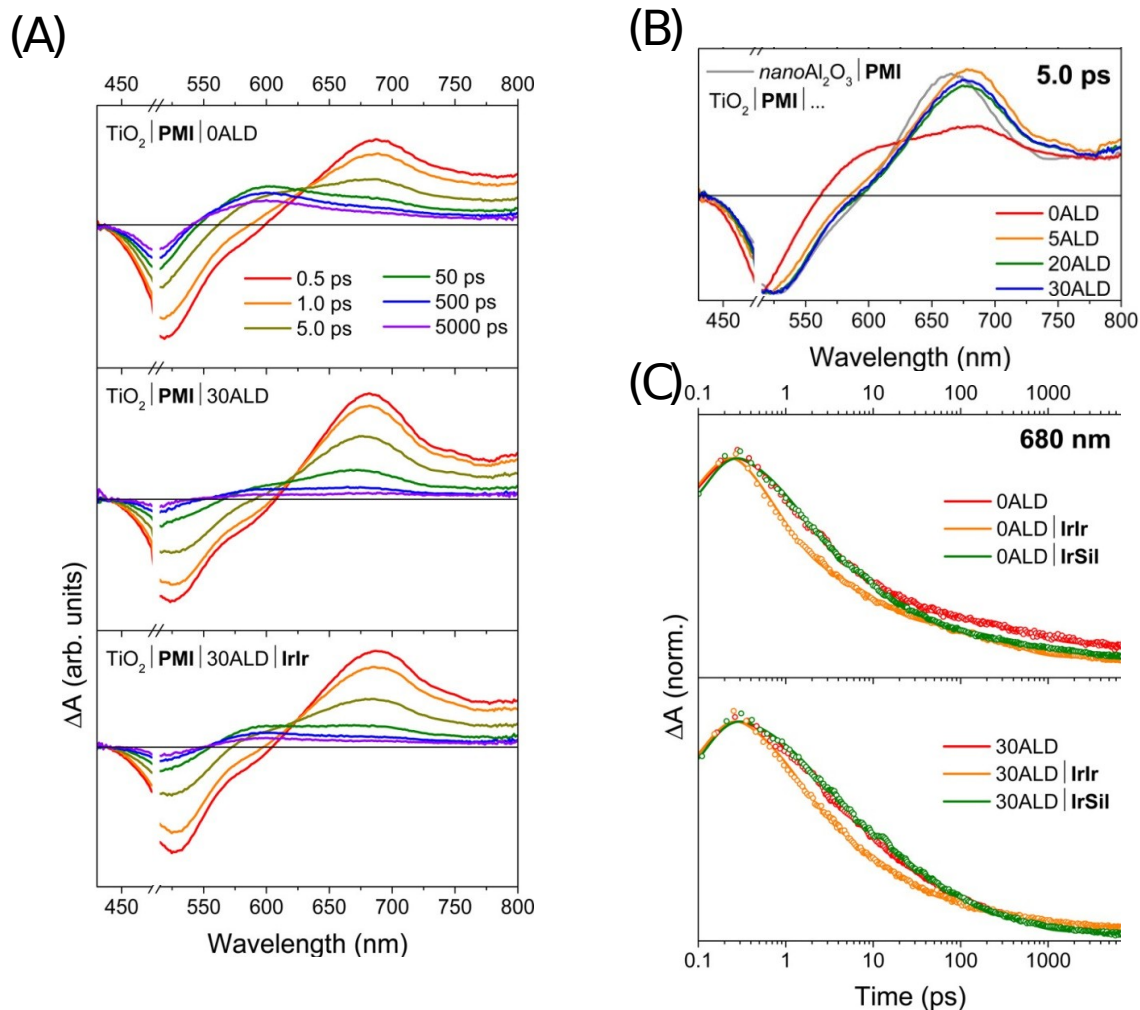
Figure 10: (A) Femtoseconds transient absorption spectra of TiO_2/PMI/0ALD, TiO_2/PMI/30ALD, and TiO_2/PMI/30ALD/IrIr upon excitation at 495 nm. (B) Corresponding transient absorption spectra of TiO_2/PMI at 5 ps with varying Al_2O_3 thickness. Only the first few ALD cycles contribute to the slower charge injection process. (C) Single-wavelength kinetic traces (circles) and fits (lines) at 680 nm of TiO_2/PMI/ALD/catalyst with 0ALD (top) and 30 ALD (bottom) with and without IrIr and IrSil catalyst, showing faster charge separation in the IrIr case. Reproduced with permission from J. Phys. Chem. C **121**, 3752 (2017). Copyright 2017
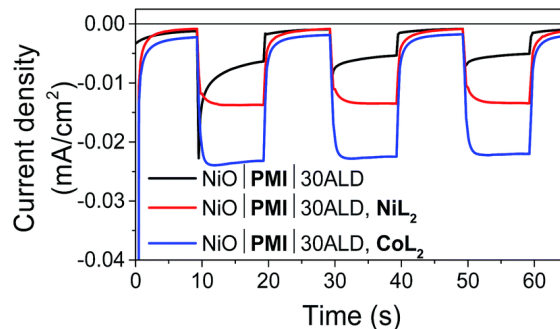
Figure 11: (A) Schematic of nanostructured NiO electrode with a modified perylene-3,4-dicarboximide chromophore that is stabilized against degradation by ALD of Al_2O_3 layers. The photoelectrochemical behavior of the electrodes in the presence of CoL_2 and NiL_2 molecular proton reduction catalysts reveals reduction of both catalysts under evolution of H_2. (B) Current density measurements with three 10 s light on/off cycles with 0.40 V applied bias on a single NiO/PMI/30ALD working electrode without catalyst (black trace) and after addition of 0.5 mM NiL_2 (red) or 0.5 mM CoL_2 (blue).
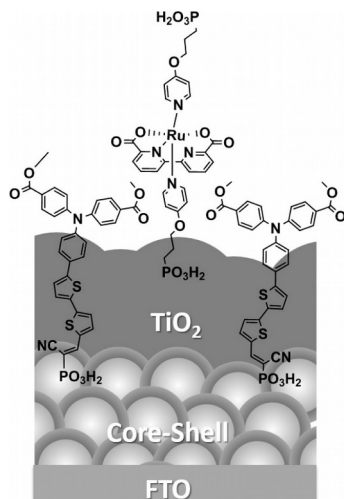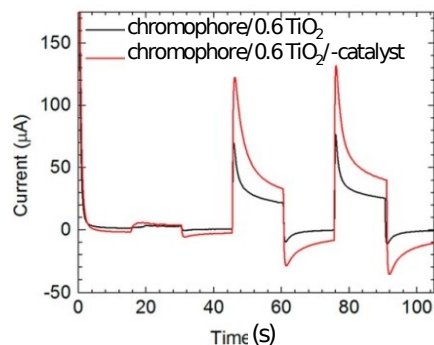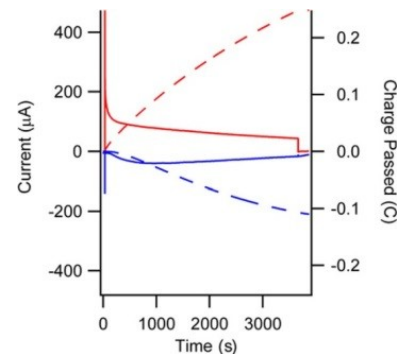
Figure 12: (A) Illustration of the layered, co-loading strategy for the organic light absorber anchored on the core/shell surface. Following ALD casting of 0.6 nm TiO_2, the water oxidation catalyst $[Ru(bda)(4\text{-}pyrCH_2PO_3H_2)_2]$ (pyr = pyridine; bda = 2,2′-bipyridine-6,6′-dicarboxylate) is anchored by phosphonate group on top of the TiO_2 layer. (B) Red trace: Photocurrent−time traces with 445 nm illumination: FTO/nanoITO/4.5 nm TiO_2/-chromophore/0.6 nmTiO_2/-catalyst in argon-saturated pH 4.6 solution (red trace). Black trace: Same construct in the absence of catalyst. Photoelectrochemical data were obtained at 15−30 s (7.8 mW), 45−60 s (49 mW), and 75−90 s (90 mW). Reproduced with permission from ACS Appl. Mater. Interfaces 9, 39018 (2017). Copyright 2017 American Chemical Society. (C) Current and charge passed from a collector−generator cell, SnO_2/TiO_2/-chromophore/0.7 nm Al_2O_3/-catalyst under 1 sun illumination for 3600 s. The solid traces show photocurrents, and the dashed lines show the charge passed for the
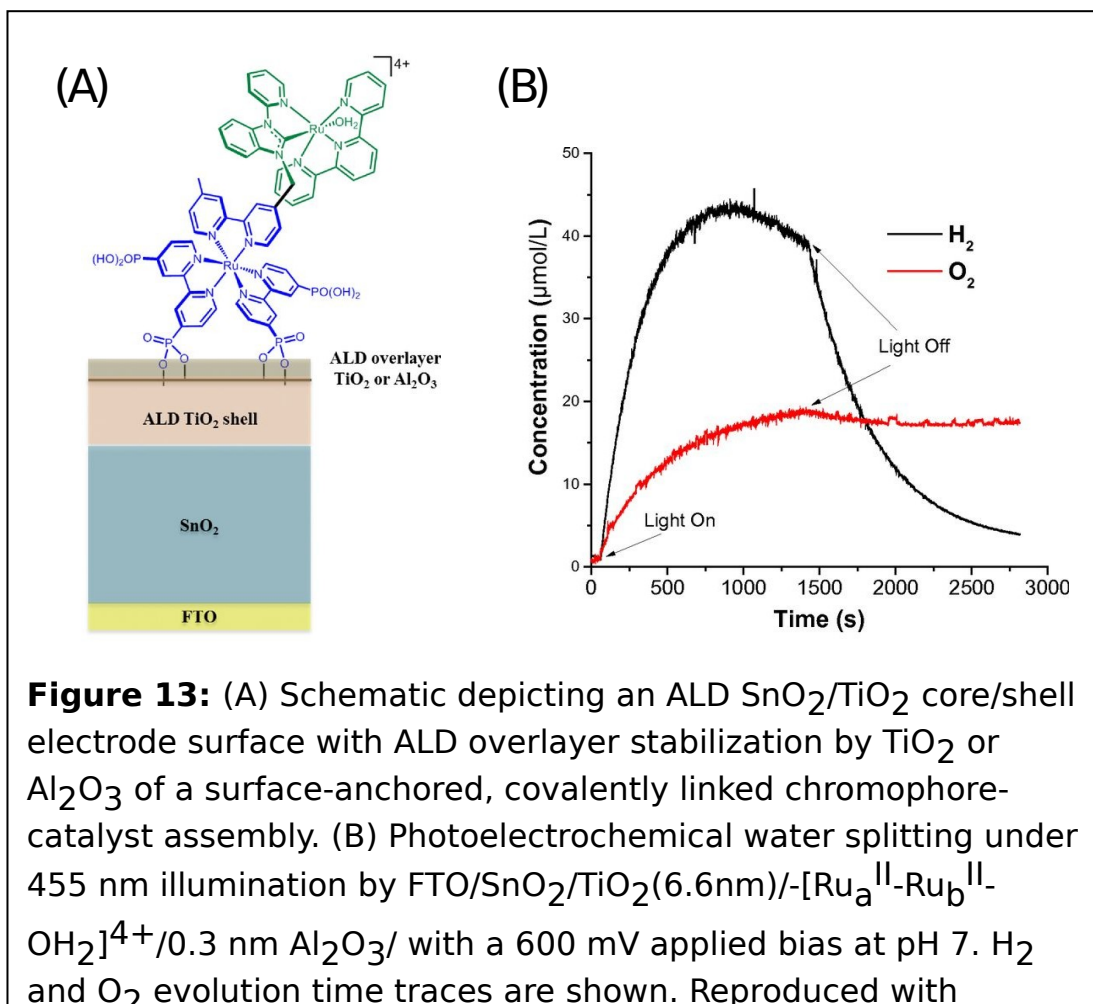
Figure 13: (A) Schematic depicting an ALD SnO$_2$/TiO$_2$ core/shell electrode surface with ALD overlayer stabilization by TiO$_2$ or Al$_2$O$_3$ of a surface-anchored, covalently linked chromophore-catalyst assembly. (B) Photoelectrochemical water splitting under 455 nm illumination by FTO/SnO$_2$/TiO$_2$(6.6nm)/-[Ru$_a^{II}$-Ru$_b^{II}$-OH$_2$]$^{4+}$/0.3 nm Al$_2$O$_3$/ with a 600 mV applied bias at pH 7. H$_2$ and O$_2$ evolution time traces are shown. Reproduced with